Title

Characterization of the atomic-level structure of γ-alumina and (111) Pt/γ-alumina interfaces

Authors

Clauser, AL

Sarfo, K Oware

Giulian, R

et al.

Publication Date

2023-02-01

DOI

10.1016/j.actamat.2022.118609

Characterization of the atomic-level structure of γ-alumina and (111) Pt/γ-alumina interfaces

A.L. Clauser,[a] K. Oware Sarfo,[b] R. Giulian,[c] C. Ophus,[d] J. Ciston,[d] L. Árnadóttir,[b] and M.K. Santala[a,1]

[a]*School of Mechanical, Industrial, and Manufacturing Engineering, Oregon State University, Corvallis, OR, USA*

[b]*School of Chemical, Biological, and Environmental Engineering, Oregon State University, Corvallis, OR, United States*

[c]*Institute of Physics, Federal University of Rio Grande do Sul, Porto Alegre, Brasil*

[d]*National Center for Electron Microscopy, Molecular Foundry, Lawrence Berkeley National Laboratory, Berkeley, CA, United States*

Abstract

The atomic-level structure of platinum/γ-alumina interfaces is characterized in a model system of dense γ-alumina embedded with faceted Pt NPs produced by implantation of platinum ions into sapphire followed by thermal annealing in air at 800°C. Aberration-corrected scanning transmission electron microscopy (STEM) was used to collect atomic-resolution images, which are compared to STEM image simulations of two experimentally-based bulk models of γ-alumina by Smrčok *et al*. and Zhou and Snyder. A density functional theory (DFT) based model of (111) interfaces with different chemical terminations (O, Al_1, Al_2) of the γ-alumina developed by Oware Sarfo *et al.* is also compared to experimental STEM data from Pt/γ-alumina interfaces. The Smrčok γ-alumina model provides a better fit than the Zhou structure to the bulk of the γ-alumina. The oxygen-terminated Oware Sarfo model best fits the experimental data and is a very good model close to the interface. However, the fit of the interface model to the experimental data is poorer beyond the third atomic layer in the γ-alumina. This is attributed to compromises required in the design of the model to limit the cell size and computational time for DFT calculations. Understanding the accuracy and limits of the structural models of γ-alumina and Pt/γ-alumina interfaces is important to further the understanding of the structure/property relationships in this system.

Keywords: alumina; platinum; interface structure; atomic structure; STEM (scanning transmission electron microscopy)

[1] Author to whom correspondence should be addressed. Electronic mail: melissa.santala@oregonstate.edu

1. Introduction

Pt nanoparticles (NPs) supported by γ-alumina (γ-Al_2O_3) is a heterogeneous catalyst used in many applications, including catalyst coatings for methane combustion in microreactors, the production of high-octane gasoline from linear alkanes, and CO chemisorption [1-4]. The NP-support interactions impact important properties of this system [5], for example, the Pt NP size and morphology can affect the activity and reaction rate of catalytic CO electro-oxidation [6] and strong metal-support interactions are necessary to sustain high activity catalysis [7]. Because of its technological importance, the structure of the Pt/γ-alumina system has been extensively studied [2, 5, 8-11] including the use of transmission electron microscopy (TEM) to characterize NP shape, size, and distribution, and the relationship of the Pt to the γ-alumina, e.g. [5, 7, 12-15]. Scanning transmission electron microscopy (STEM) with electron energy loss spectroscopy (EELS) has been employed to characterize the bonding at the interfaces [15]. Spectroscopic methods like EELS can be used to generate chemical and bonding data with probe sizes as small as 0.1 nm, fine enough for atomic resolution analysis. However previous electron microscopy studies have not resolved the atomic-level structure across the Pt/γ-alumina interface. Beam damage can be an issue for atomic resolution STEM experiments, as transition aluminas can quickly become damaged during atomic resolution microscopy [16]. In addition, the structural characterization of γ-alumina is intrinsically challenging, because of its structural disorder, often poor crystallinity, and the topotactic dependence of its structure on its precursor. These factors have resulted in multiple proposed structural models for γ-alumina [17-26].

Gamma-alumina is a metastable transition phase, which may be formed by diverse processing methods, including dehydration of boehmite [18, 27-30], plasma spraying [31], re-

crystallization of partially amorphized sapphire (single crystal α-Al_2O_3) wafers [32, 33], oxidation of NiAl [34, 35], and the reaction of SiAlON ceramics with liquid steel [26, 36]. Commercially, γ-alumina is formed when an aluminum hydroxides, often boehmite ore (AlOOH), are calcined at 800°C. Boehmite-derived γ-alumina is formed when water is driven out of the structure causing a collapse of (001) layers of boehmite [20] and may impart a residual tetragonality inherited from the parent structure [18], though the γ-alumina unit cell is usually described as cubic.

In this work, γ-alumina is formed by re-crystallization of partially amorphized sapphire. The transition aluminas that develop on the amorphous→ γ→ δ→ θ→ α-alumina transformation path progress mainly by rearrangement of Al within the oxygen sublattice. The γ, δ, and θ forms possess a face-centered cubic (FCC) oxygen sublattice with a spinel-like distribution of Al cations. To maintain the Al_2O_3 stoichiometry, only a fraction of the O interstitial sites are occupied by Al. The differences in the distribution of the Al differentiates these transition aluminas. Gamma-alumina has been determined to have 25-30% of Al atoms on tetrahedral O interstices (Al_t), whereas δ-alumina has 37.5% and θ-alumina has 50% of the Al on Al_t positions [37]. As the processing temperature increases, Al migrates from octahedral sites (Al_o) to Al_t sites in the transition forms, but at higher temperatures (~1000°C), θ-Al_2O_3 transforms to α-alumina, the most stable form, which has a hexagonal-close-packed O-sublattice with all the Al on Al_o sites.

1.1. Structural models of γ-alumina

Several models for the structure of γ-alumina have been proposed, including a widely-cited defected cubic spinel model by Zhou and Snyder [19] , a cubic spinel model by Smrčok *et al.* [26], a widely-used density functional theory (DFT)-based non-spinel model by Digne *et al.* [21,

24], a distorted tetragonal spinel by Paglia *et al*. [23] which does not restrict Al cations to spinel positions, a DFT-based model by Pinto *et al*. which was developed to model surface behavior and which also proposed non-spinel cation sites dominated by five-coordinated aluminum and some tetrahedral Al [25], among others [17, 22]. Recent work by Ayoola *et al*. [35] evaluated the Smrčok [26], Paglia [23], Digne [24], and Pinto [25] models of γ-alumina by comparing them to x-ray diffraction (XRD) and TEM data of γ-alumina grown from single crystal NiAl (110) wafers. They found the Smrčok model to be the best fit based on comparison of experimental and simulated diffraction data. They did not consider the Zhou model, but this model was found to be a good fit to electron diffraction data of γ-alumina derived from the recrystallization of partially amorphized sapphire by Clauser *et al*. [33].

In this work, the bulk γ-alumina structure is compared to the Zhou and Smrčok models, which differ primarily in the positions the Al atoms occupy. The Zhou [19] model is based on the Rietveld refinement of neutron diffraction and XRD data from boehmite-derived γ-alumina powder calcined at 873 K (600°C). The Smrčok structure was developed from XRD data from γ-alumina whiskers produced in the reaction of SiAlON with liquid steel [26, 36]. Figure 1 and

show the unit cells and structural data for both models. Both have an $Fd\bar{3}m$ defective spinel structure consisting of approximately eight formula units of $Al_{2\frac{2}{3}}O_4$, as in the conventional formula for the defective spinel of $\ominus_{2+2/3}Al_{21+1/3}O_{32}$, where $\ominus$ is a cation vacancy in the spinel structure. They both have an FCC oxygen sublattice with two types of alternating [38] Al layers between the close-packed {111} O layers. One Al layer is composed of Al_o in the 16d site and the other layer is composed of a mixture of Al_o, Al_t, and, in the Zhou model, 32e "quasi-octahedral" sites. This second layer will be designated as $\{111\}Al_{mix}$ for both models. A set of

{111} O-Al_o-O-Al_{mix} layers are indicated on both unit cells in Figure 1. The Smrčok model assumes a higher occupation of Al in the octahedral 16d site than the Zhou model and thus has a higher occupancy in the Al_o layer. Both models have a similarly high occupancy of the 8a tetrahedral site. The Smrčok model has a 63:37 Al_o to Al_t ratio with 6% of Al in two sparsely occupied non-spinel octahedral and tetrahedral sites 16c and 48f.

1.2. Production of Pt NPs in γ-alumina

When Pt NPs are dispersed on γ-alumina surfaces (as for catalysis), the particles take on a variety of orientation relationships with the substrate and the character of the interfaces may be impacted by impurities and the degree of crystallinity of the γ-alumina. This introduces enormous complexity in the atomic-level characterization of the structure of Pt/γ-alumina interfaces. To facilitate atomic-level structural characterization, in this study, clean interfaces with a specific interfacial relationship were produced in a model system consisting of faceted, oriented Pt NPs embedded in dense γ-alumina by implantation of Pt into sapphire followed by thermal annealing. Ion implantation of crystalline oxides with other species followed by thermal annealing can be used to generate epitaxially grown oxides with embedded NPs with control of precipitate size distribution, particle orientation, and purity of the system [39, 40]. Accumulated damage caused by high energy implantation of species into sapphire creates an amorphous region near the surface of an implanted wafer, which may subsequently be re-crystallized into the transition forms and be used to study crystallization kinetics of the alumina and the properties of the precipitated NPs in contact with the alumina [32, 41].

The temperature required for amorphous alumina to crystalize to γ-alumina depends on the processing of the alumina, but can occur at temperatures as low as 600°C [42]. The presence of γ-alumina has been reported at temperatures up to 1000°C [42, 43], though conversion to other

transition aluminas, such as δ-alumina [44], may occur well below that temperature. High-energy implantation of sapphire with Pt followed by thermal annealing in air at 1173 K (800°C) has been found to result in Pt NPs in γ-alumina with no δ-alumina detectable with XRD or selected area electron diffraction and the NPs take the cube-on-cube orientation relationship of $(111)_{Pt}\|(111)_{\gamma}$; $[1\acute{1}0]_{Pt}\|[1\acute{1}0]_{\gamma}$ [33]. The lattice misfit in this case is relatively small, ~1%. Small Pt NPs with this orientation are nearly tetrahedral, bound by {111} facets, whereas larger NPs may be cubo-octahedral with large {111} facets and relatively small {200} facets. The high prevalence of the {111} facets motivated a DFT-based study of the structure and thermodynamic stability of Pt/γ-alumina interfaces with this interfacial relationship [45], briefly reviewed in the following section.

1.3 Structural model of the Pt/γ-alumina interface

There have been many models of single atoms [15, 46] or small clusters of Pt [7, 11, 47] on γ-alumina, but few of extended interfaces [45]. The predominance of the {111} facets observed by Clauser *et al*. was used as guide for a DFT-based study by Oware Sarfo *et al*. [45] of the structure and relative thermodynamic stability of Pt/γ-alumina interfaces with the $(111)_{Pt}\|(111)_{\gamma}$; $[1\acute{1}0]_{\gamma}\|[1\acute{1}0]_{Pt}$ interfacial relationship with different chemical terminations (O, Al, and Al_2) of the γ-alumina. The O-terminated interface was found to be the most thermodynamically stable at 1173 K and an oxygen partial pressure (pO_2) of 0.2, the processing conditions used in [33] and in this work. Here, the Oware Sarfo interface model [45] is compared to experimental atomic-resolution microscopy images through image simulations. The starting point for the γ-alumina in the Oware Sarfo model was the DFT-based model by Digne *et al*. [24], which is monoclinic and is based on a computational study by Krokidis *et al*. [20] modelling the conversion of boehmite

to γ-alumina during calcination. The Digne model was developed for surface studies and used the lowest energy structure of the Krokidis simulation with 25% of Al cations in Al_t positions [24]. The model consists of eight Al_2O_3 formula units and thus is significantly (25%) smaller than the defective spinel models. It is widely used in DFT studies due to the simplicity of the cell, lack of partial occupancies, and successful benchmarking against experimental data of mainly surface-sensitive properties.

2. Methods

To create a model material with a high density of Pt/γ-alumina interfaces with one interfacial orientation, Pt NPs were precipitated in a γ-alumina matrix by annealing single crystal optical grade (99.99%) α-Al_2O_3 wafers that had been implanted at room temperature with nominally 1×10^{17} Pt^+/cm^2 accelerated to 600 keV. The wafer was cut with the $[0001]_\alpha$ normal to its face and it was implanted at an angle 7° off the normal to avoid channeling. These implantation parameters amorphize a sub-surface region of the sapphire wafer and result in a peak distribution of Pt 110 nm below the surface. Characterization of the as-implanted wafer is described elsewhere [33]. Pieces of the implanted wafer were annealed at 800°C for 500h in air, which is long enough to enable a transition of amorphous alumina to γ-alumina and the formation of faceted Pt NPs [33]. The annealed wafer pieces were prepared in cross section for TEM characterization by bonding two pieces of wafer together using M-bond 610 epoxy adhesive, sectioning them, thinning sections to $\approx$ 160 - 180 μm thick, and polishing to a 0.25 μm diamond paste finish on one side. Samples were then dimpled to < 20 μm on the other side and polished to a 0.25 μm finish before being ion milled with argon to electron transparency.

STEM data was collected on the TEAM 1 microscope, a double probe-corrected FEI Titan at the National Center for Electron Microscopy (NCEM) facility of the Molecular Foundry, operated at 300 keV. STEM images were collected with a probe semi-angle of 17 mrad and 115 mm camera length along the $[110]_{Pt}$ and $[211]_{Pt}$ zone axes. High angle annular dark field (HAADF) and annular bright field (ABF) detectors were used to collect orthogonally scanned HAADF/ABF image pairs. The collection angles are 62 – 310 mrad and 5 – 27 mrad for the HAADF and ABF, respectively. The orthogonal STEM image pairs were used to perform drift correction to reduce the effect of nonlinear drift using an algorithm developed by Ophus *et al.* [48]. The STEM probe step size (pixel size) varies with magnification and is given in the captions of figures with STEM images. To mitigated beam damage, once a very thin area with Pt NPs was located on a sample, final alignments were performed on an adjacent area before the orthogonal image pairs were collected, minimizing the time the specimen was exposed to the beam.

Simulated STEM images of the Zhou, Smrčok, and the Oware Sarfo models on the [110] and [211] zone axes were generated using Prismatic [49], to simulate STEM images, for comparison to experimental images. The Smrčok model used in the simulation was taken from the .cif file accompanying reference [26]. Slabs of the structures were constructed to have parallel surfaces normal to the experimental zone axes (also the electron beam direction). The structures used to simulate the Smrčok [110] and [211] zone axis models are 22.4 and 15.50 nm thick, the Zhou [110] and [211] models are 23.82 and 15.83 nm thick, and the Oware Sarfo [110] and [211] models are 7.82 and 9.70 nm thick in the beam direction, respectively. The exact sample thickness was not known at any point, but the values used for the simulations are considered reasonable estimates. The Al_1- and Al_2-terminated models are shown in Figure S1 of the

Supplemental Material. The O-terminated Oware Sarfo interface model used in the simulations appears in Figure 6 and 7. The parameters used for Prismatic simulations were chosen to represent the imaging conditions of the TEAM 1.0 microscope using, 300 keV accelerating voltage, and 17 mrad probe semi-angle, and 5 - 27 mrad ABF. The .pdb files for the slabs used in the Prismatic simulations are available in the Supplemental Material.

Atomap, a Python library created for the analysis of atomic resolution STEM images [50], was used for 2-D Gaussian fitting of atomic columns of average experimental STEM HAADF images and the simulated micrographs. It was also used to aid in identifying symmetry axes.

3. Results and discussion

A HAADF and ABF STEM image pair in Figure 2 gives an overview of γ-alumina with several Pt NPs. The alumina is multiply twinned along {111} planes and the twins are labeled 1 – 4 and the boundaries are marked with white line in Figure 2(a). Twins 2 and 4 are oriented such that $(220)_{\gamma}$ planes are horizontal in the figure. Imaging is down a shared {110} zone axis of the γ-alumina twins and Pt NPs, as shown in the indexed fast Fourier transform (FFT) of the HAADF (Figure 2(c)). The NPs have the orientation relationship of $(111)_{Pt}\|(111)_{\gamma}$; $[1\acute{1}0]_{Pt}\|[1\acute{1}0]_{\gamma}$ within the γ-alumina. The small NPs are tetrahedral or truncated tetrahedra mainly bound by {111} facets. Larger NPs may be cubo-octahedral, as described previously [33]. The $\{111\}_{Pt}$ facets viewed edge on in the HAADF image (Figure 2(a)) have the brightest Pt atomic columns, since the intensity in the HAADF increases with increasing thickness and atomic number. The tetrahedral particles taper off in thickness in the [220] direction which causes decreasing brightness in the Pt columns of the HAADF image [33]. The ABF STEM image (Figure 2(b)) shows greater contrast in the alumina matrix than the HAADF, resulting in additional intensities

in the FFTs, *cf.* Figure 2(c,d). Throughout the alumina there are bands consisting of three atomic layers of {111} planes of similar intensity separated by a gap, which is more apparent in the ABF image. The {111} planes run parallel to both the ɣ-alumina twin boundaries and to the facets of the Pt NPs. By comparison to the bulk alumina models, described in the next sections, these layers may be identified as sets of {111}O-Al_o-O layers.

3.1 Comparison of ɣ-alumina to Smrčok and Zhou models

The area of the ABF image marked by a box in Figure 2(b) viewed down a [110] zone axis is reproduced in Figure 3(a) for comparison to STEM ABF image simulations of the Smrčok and Zhou models in Figure 3(b) and (c). Both models have a fully occupied O sublattice and thus the O atomic columns have similar uniform intensity[2] in the image simulations. Both models have Al in the 16d position, which forms the {111} Al_o layer and occupies sites in the {111} Al_{mix} planes, but the Smrčok model has a higher occupancy of the 16d position, which results in Al columns in the Al_o layer that have nearly the same intensity as the O columns. The models differ in simulated intensity of Al columns in Al_t positions due to differences in occupation. The presence of quasi-octahedral Al in the Zhou model gives rise to a smeared appearance of some atomic columns in the simulated images, whereas the Smrčok model has clear Al_t and non-spinel Al_o columns between (220) planes. Although distinct in the simulated images, the Al_t are close enough to the O columns that they may not be resolved in experimental images.

The simulated STEM images in Figure 3(b,c) show a convenient visual unit of O-Al_o-O columns that appears as a horizontal row of three spots, that are marked by boxes on the simulated images and corresponding models. The O-Al_o-O columns form diagonal bands along {111} planes that are separated by an apparent gap where there is a {111}Al_{mix} layer. Of the two

[2] For the ABF STEM images lower intensity indicates higher occupancy in an atomic column.

models, the Al occupancy in the Smrčok model results in a more uniform intensity of all columns in the diagonal band of O-Al_o-O layers, which better matches the intensities in the experimental image. Although there is variability in the intensities in ɣ-alumina in the experimental images, the key features of the dense plane of units of three atomic columns that runs diagonally with {111} planes separated by less densely occupied (111) planes, allow us through comparison with the models to differentiate the O from the Al columns. The banding of three nearly uniform O-Al_o-O {111} planes on the [110] zone axis is consistent with the Smrčok model which has higher occupancy of Al_o layers and lower occupancy Al_{mix} layers than the Zhou model.

Figure 4 shows a ABF/HAADF STEM image pair of γ-alumina with small Pt NPs viewed down a [211] zone axis. Still focusing on the matrix, there appear to be two variants in the alumina. An area that contains both variants is marked by dashed boxes in Figure 4(a, b) and it is compared to the Zhou and Smrčok models and image simulations in Figure 5. On the {211} zone axis, the O-Al_o-O columns form vertical groups of three distinct atomic columns (marked with a box) in the image simulations, whereas the O-Al_{mix}-O columns form a smeared bar of more uniform intensity (marked with an oval), in which the atomic columns are not resolved. The image simulations of both the Smrčok and Zhou models (Figure 5(b,c)) have a brick-like arrangement of O-Al_o-O units and O-Al_{mix}-O with these units separated interstitial sites with low occupancy of Al, $□_i$, similar to the lower left side of the experimental images. The variant on the upper right side of Figure 5(a,b) appears to have O-Al_o-O units aligned in horizontal rows and an apparent increase in occupancy between the O-Al_o-O layers. In both regions the comparison with the models aids in the identification of the {111} layers of the oxygen sub-lattice. Local changes in the apparent ordering of the O-Al-O units seen in the γ-Al_2O_3 [211] zone axis are not readily

apparent in the [110] zone axis images. Using the Smrčok model as a reference, the variant in the upper right may have locally higher occupancy in the 16c position (orange branches in the Figure 5(b) and 1(b) models). However, it is also possible that the appearance of the variant with linear stacking of O-Al-O is due to defects through the thickness of the specimen that disrupts alignment of the Al, which would result in apparent averaging of the occupancy of the Al positions. This would not require a defect in the O sub-lattice, but simply a local shift in the Al occupancy of the Al_{mix} layers through the thickness of the TEM sample. For example, a shift of the Al in the mixed layers by $[04\acute{4}]$ in the Figure 5(b) would move the Al encircled by the oval to a $\square_i$ column. The latter interpretation is supported by the finding that the brick-like stacking is only apparent in the very thinnest portions of the TEM specimens.

The lattice parameter for γ-alumina and Pt NPs were measured in the STEM images and the results are compared to the Smrčok and Zhou models and bulk Pt [51] in Table 2. The measured value for γ-alumina is ~4% larger than for both the Smrčok and Zhou models. Given the purity of the γ-alumina precursor (optical grade sapphire) and the introduction the Pt through ion implantation, which accelerates almost exclusively Pt^+ ions into the specimen, it is unlikely that this is due to impurities in the precursor materials. The implanted Pt and the amorphized alumina layer are tens of nanometers from the surface of the sapphire, though this does not isolate these layers from the furnace environment. For example, Pt NPs formed in amorphous silica by ion implantation followed by annealing in forming gas (95% N_2, 5% H_2) have a lattice parameter larger than the bulk value due the incorporation of hydrogen, even though most NPs are more than 1 μm below the silica surface [52, 53]. It has also been observed that co-implantation of Pt and Co into sapphire to a similar depth as in these experiments, followed by annealing in

forming gas (96% N_2, 4% H_2) results in the formation of chemically-ordered CoPt NPs, whereas annealing in an O_2 results in the formation of Pt and Co_3O_4 NPs [54]. Here, the specimens were annealed in air, which has an H_2 content in the parts per million range, thus incorporation of hydrogen is not expected. Oxygen is available to diffuse into the specimen but is not expected to result in a larger γ-alumina lattice parameter relative to other processing methods. This it is unlikely that the relatively large lattice parameter of γ-alumina is due to an impurity effect.

Considering both the lattice parameter, and more significantly the distribution of Al, the Smrčok structure (which has a larger lattice parameter and higher occupancy of Al_o layers) provides a better fit than the Zhou model to experimental data. The Smrčok structure, which is based on γ-alumina produced in reactions between β-SiAlON and steel [26, 36] may be a better fit to γ-alumina derived from amorphized sapphire and γ-alumina derived from oxidation NiAl single crystals [35], because the precursors are completely anhydrous (or for one specimen in [36], mostly anhydrous). The structures of γ-alumina derived from anhydrous precursors may be more similar to each other than to γ-alumina derived from calcined boehmite, which is the basis of the Zhou model.

The measured lattice parameter for Pt is 6% larger than the bulk value, as shown in Table 2. As discussed above, it is unlikely that the expansion of the lattice parameter is due to the incorporation of hydrogen or other impurities. The lattice parameter of NPs may differ from the bulk due to capillary effects caused by the presence of a surface or interface, as observed experimentally for Pt [55-60], but the nature of the interface bounding the NP is important. The lattice parameter for small Pt NPs (< 4 nm) has been observed to be smaller than the bulk several percent by multiple researchers [55-57, 59-61] as expected from calculation for Pt NPs (with bare surfaces) [62-64], but lattice expansions have been observed for Pt NPs covers with an

oxide layers [58, 59] or thiol ligands [61]. Here, contact with, and bonding to, the ɣ-alumina matrix along a coherent, faceted interface may cause the increase in the Pt lattice parameter relative to the bulk. ~~The measured value for ɣ-alumina is ~4% larger than for both the Smrčok and Zhou models. Considering both the lattice parameter, and more significantly the distribution of Al, the Smrčok structure provides a better fit than the Zhou model to experimental data.~~

3.2 The structure of the (111) Pt/ɣ-alumina interface

Figure 6(a) shows a drift-corrected ABF image of a cubo-octahedral NP bound by four {111} facets viewed edge-on along a [110] zone axis. The FFT (inset) shows a pattern consistent with Pt in twinned γ-alumina grains. All the {111} Pt/ɣ-alumina facets have a similar structure close to their interfaces, though some variation in the alumina may be attributed to twinning around the NP, slight changes in orientation relative to the [110] direction, and structural variation in the alumina. The boxed area in Figure 6(a), which has ɣ-alumina exactly on zone axis and well-resolved atomic columns at the interface, is reproduced in (b). The γ-alumina at the interfaces with Pt in the ABF image show a row of three dark columns (marked with a box), which match the O-Al_o-O groups marked by boxes in model and image simulations of the Oware Sarfo DFT O-terminated interface shown in Figure 6(c). Notably, all the Al in the layer adjacent to the O at the interface relaxed into the octahedral positions in the Oware Sarfo model, even though the initial unrelaxed structure had Al in both octahedral and tetrahedral sites in this layer [45]. The Al_1- and Al_2-terminated interface models and image simulations are available in the Supplemental materials for comparison, but both are qualitatively poor matches to the experimentally observed structure at the interface. In the O-terminated model and experiment, the Pt sits directly on top of the terminating layer oxygen in the ɣ-alumina. In addition, there is a good structural match down to three layers of atoms into the alumina, Pt-O-Al_o-O. Beyond that,

all the {111} Al layers have mixed octahedral and tetrahedral occupancy in the O-terminated Sarfo model, rather than alternating between Al_o and Al_{mix} planes in the bulk models, the latter of which more closely match experimental images. The Oware Sarfo model also does not maintain the high alignment of the O and Al_o columns in the [110] direction, although the atomic columns of the O-Al_o-O layers are well resolved in the STEM images as in Figure 2(b) and Figure 6(a).

Figure 7(a) shows the Pt/γ-alumina interface from the boxed area in Figure 4(b) viewed on a [211] Pt zone-axis compared to the O-terminated Oware Sarfo model. In this orientation only one horizontal interface of each Pt tetrahedron in the STEM image is parallel to the electron beam. The appearance of the first three O-Al_o-O {111} layers in the simulated image are consistent with the experiment in that there are vertically align grouping of three atomic columns. A group of O-Al_o-O columns is marked by boxes in each part of Figure 7. (The Al_1- and Al_2-terminated models and image simulations are also available in the Supplemental materials for this orientation.) In the experimental image the second alumina {111} layer from the interface, corresponding to an Al_o layer in the simulation, is light relative to the adjacent layers, however in the simulation, the columns in the Al_o are either darker or appear to be unoccupied.

When the Oware Sarfo model is viewed along the [211] direction, there are adjacent unoccupied interstitial Al columns, $□_i$, direction that do not appear in the bulk models of γ-alumina or in the experimental images. These empty interstitial columns, that are not seen in the experiment or bulk models, are a consequence of the constraint that the DFT model cannot have partially occupied sites, but otherwise must satisfy the same stoichiometry and structural constraints as the other models, thus the Al cannot be distributed over as many sites. The adjacent $□_i$ columns appear in the model and simulated images as large gaps between in

alternating {111} planes of Al; examples are labelled with $\square_i\square_i$ in Figure 7(b). In addition, the {111} plane of Al closest to the interface is occupied by Al_o with a single $\square_i$ column, although experimental interfaces viewed from the [211] zone-axis do not have low occupancy interstitial positions in the layer of Al closest to the interface.

For a quantitative evaluation of the fit of the interfacial models to the experiment, the distance between the terminal-Pt and first O layer in the Oware Sarfo model interfaces (O-, Al_1-, and Al_2-terminations) is compared to the experimental images, in an approach similar to that taken by Ophus et al. [65] for the structural characterization of Pt/α-Al_2O_3 interfaces. This approach is taken, because in both the image simulation of the models and the experimental images, highly occupied Al_o and fully occupied O columns are better resolved that the Al_t columns and the lower occupancy Al_o and Al_{mix} columns. Thus, there is more certainty regarding the position of O columns than the Al positions in the experimental images. The results of the comparison are summarized and compared to experimental Pt-O distances and standard deviations in Table 3. The average distances and standard deviations were derived from ten separate measurements of the Pt-O distance on seven different NP interfaces from five different drift-corrected STEM images. By this measure, the O-terminated model is again the best fit as the experimentally measured distance is ~5% larger, similar to the differences between the measured lattice parameters of Pt and γ-alumina when compared to the literature values. The measured distance is 14% and 37% smaller than in the Al_1- and Al_2-terminated interfaces, respectively.

Based on the qualitative and quantitative fit of the interfacial structure, the O-terminated Oware Sarfo interfacial model provides the best fit to the experimental data. This model matches the experimental images with respect to (1) the Pt positioned on top of the terminating O as

viewed from both the [110] and [211] zone axes, (2) the {111} O-Al_o-O layers at the interface, and (3) the distance between the terminating Pt and O layers. The O-terminated interface was calculated to be the most stable of the three terminations for pO_2 = 0.21 atm and temperatures ranging from room temperature to 1900 K and thus is expected to be the most stable for the processing conditions used in these experiments [45]. The bonding of Pt to oxygen on γ-alumina observed here is consistent with other spectroscopic and imaging studies of Pt on alumina [15, 65]. In the work by Ayoola et al.[15], a DFT-based structure made up of tetrahedrally coordinated Al at the surface of a γ-alumina supporting a single Pt atom required the addition of an O adatom bridge, in order to make their simulated EELS spectrum consistent with their experimental spectra from Pt NPs supported on (111) γ-alumina. In a similar study comparing DFT-based calculated structures of (111)Pt/(0001)α-alumina interfaces with O-, Al_1-, and Al_2-terminations of the α-alumina to high-resolution TEM (HRTEM) data [65] found the O-termination to be best structural match to Pt/α-alumina interfaces of embedded Pt particles processed at 1973 K in air, although the transition between the Al_1- and the O-termination was calculated to occur at 1600 K at (pO_2) = 0.2 over a large range of temperatures. The terminating Pt sits nearly on top of the terminating O on (0001)α-alumina in the model and experiment when viewed along the shared [1010]α and $[110]_{Pt}$ direction.

4. Summary and conclusions

A combination of experimental atomic-resolution microscopy with image simulation of the Zhou and Smrčok γ-alumina models and recently developed Pt/γ-alumina interfacial models were used to develop an understanding of the atomic structure of the interfaces of Pt NPs in γ-alumina. The Smrčok model was a better fit to the experimental observations of bulk structure of

ɣ-alumina derived from an anhydrous amorphous precursor than the Zhou model. Of the three chemical terminations (O, Al_1, Al_2) of Oware Sarfo interface models, the best fitting structure is O-terminated and it is calculated to be the lowest energy structure of the three terminations for the processing conditions used. The simulated O-terminated structure has Pt located directly on top of the terminating O position. Beyond the first three {111} O-Al_o-O layers at the interface the ordering of the O and Al_o in the bulk γ-alumina remains highly aligned in the experimental image, but not in the DFT models. The differences in the bulk structure are attributed to compromises required to model ɣ-alumina with DFT.

The atomic-resolution structure characterization of Pt/ɣ-alumina interfaces on faceted embedded Pt NPs provide a basis the validation of DFT-based models of the extended interfaces and reveals the shortcomings of the models. This provides a foundation for the development more geometrically complex models of supported Pt NPs on ɣ-alumina also include a vacuum or vapor phase.

Acknowledgements

This work was supported, in part, by the National Science Foundation through Grant No. 1610507. Probe-corrected STEM was performed at the National Center for Electron Microscopy (NCEM) part of the Molecular Foundry at Lawrence Berkeley National Laboratory (LBNL). Work at the Molecular Foundry was supported by the Office of Science, Office of Basic Energy Sciences, of the US Department of Energy (contract no. DE-AC02-05CH11231). A.L.C. acknowledges funding from the Department of Energy SCGSR program which supported travel to LBNL.

Figures and Tables

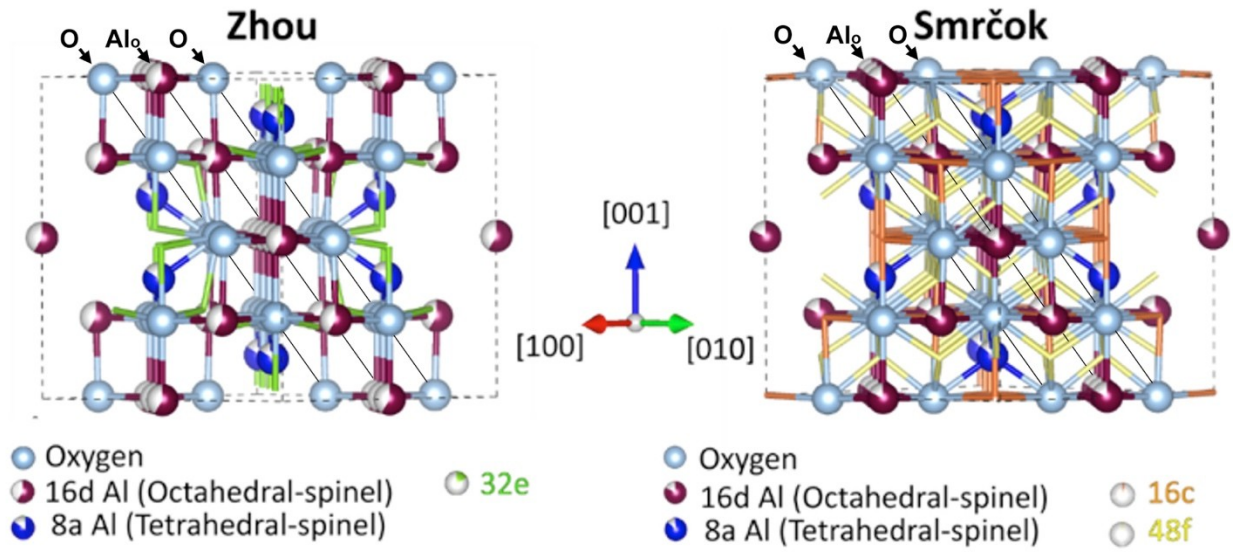

Figure 1 *Zhou and Smrčok models for ɣ-alumina. Oxygen forms an FCC sublattice in both models with Al in spinel and non-spinel positions defined by partial occupancies. For clarity, atomic sites with occupancies below 0.3 are represented colored branches rather than spheres. O, Al_o, and Al_{mix} $(1\,\acute{1}\,1)$ layers are indicated with thin solid black lines.*

Table 1 *Atomic positions for the Zhou and Smrčok ɣ-alumina models.*

Species	Site	Site description	Occupancy - Zhou model	Occupancy - Smrčok model
O	32e	FCC sub-lattice	1	1
Al_o	16d	octahedral	0.58(1)	0.816(5)
Al_t	8a	tetrahedral	0.84(2)	0.8633(5)
Al	32e	quasi-octahedral	0.17(2)	
Al	16c	non-spinel octahedral		0.028(5)
Al	48f	non-spinel tetrahedral		0.019(2)

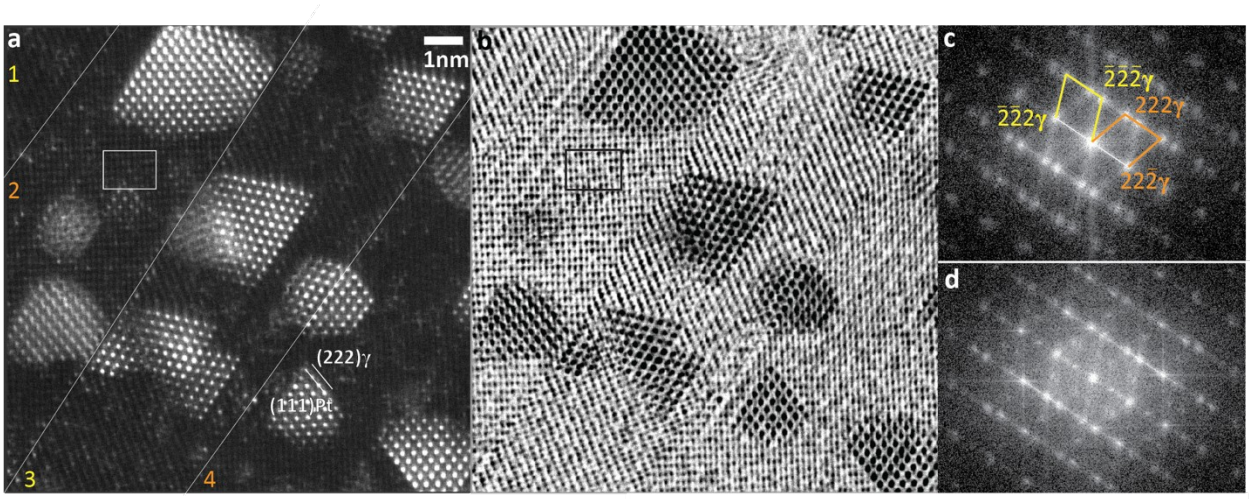

Figure 2 *Drift-corrected (a) HAADF and (b) ABF image pair showing Pt NPs embedded in multiply twinned γ-alumina down {110} zone axes (STEM probe step size: 0.0058nm). Twins on {222} alumina planes are marked with white lines (a). A unit cell of alumina marked by boxes in (a,b) is shown in detail in Figure 3. FFTs of the (c) HAADF and (d) ABF show the two twin orientations (labeled in c). Increased contrast in the alumina matrix in the ABF image results in intensities in (d) not seen in (c).*

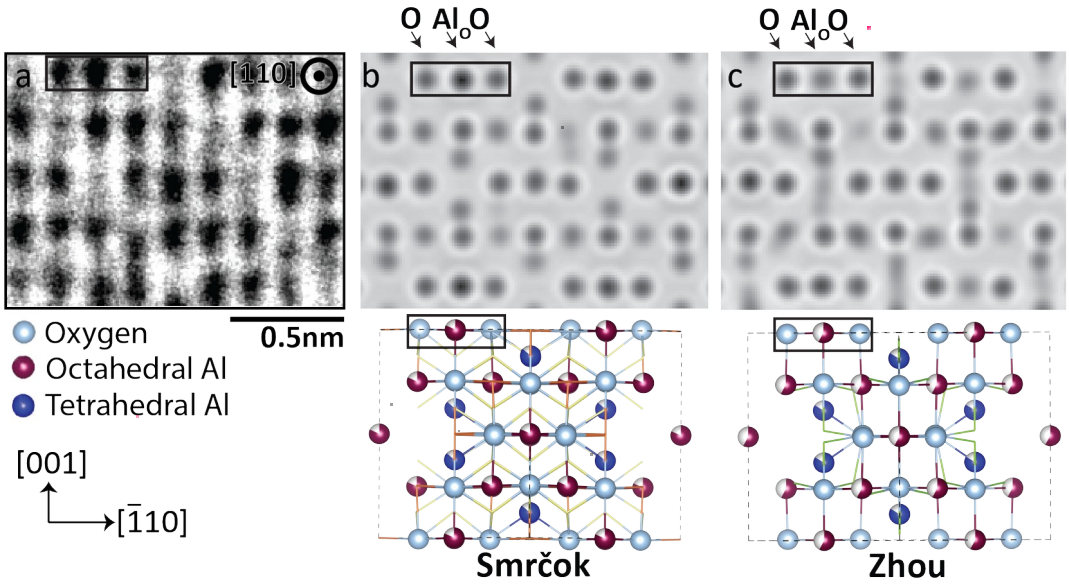

Figure 3 *(a) ABF image of a unit cell of alumina from Figure 2(b). Units made of O-Al_o-O columns are marked by boxes in the image simulations (top) and ball-and-stick models (bottom) of the (b) Smrčok and (c) Zhou models of γ-alumina. The Smrčok model results in more uniform intensity in the entire band of O-Al_o-O units and lower intensity positions mainly occupied by Al_t resulting in a better match to the experimental images.*

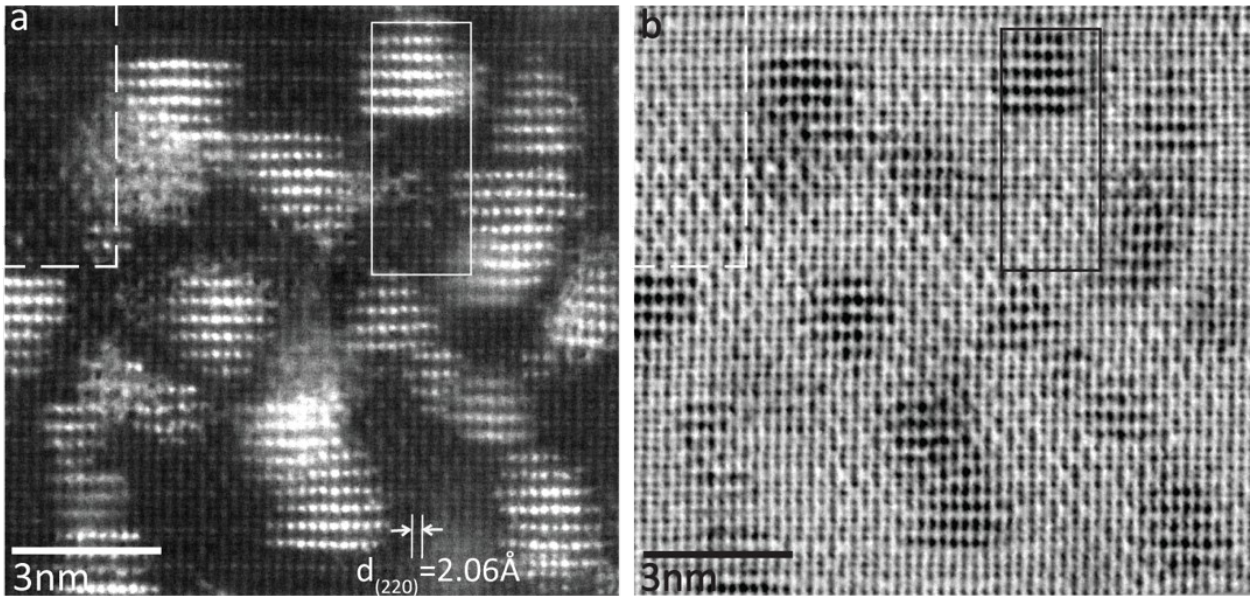

Figure 4 *Drift-corrected (a) ABF and (b) HAADF pair of Pt NPs in γ-alumina viewed on a [211] zone axis (STEM probe step size: 0.0083 nm). The {111} planes run horizontally in this image. Only one horizontal (111) Pt facet in each NP is viewed edge on. The mottled appearance in areas of (a) is due to the accumulation of material on the surface during imaging.*

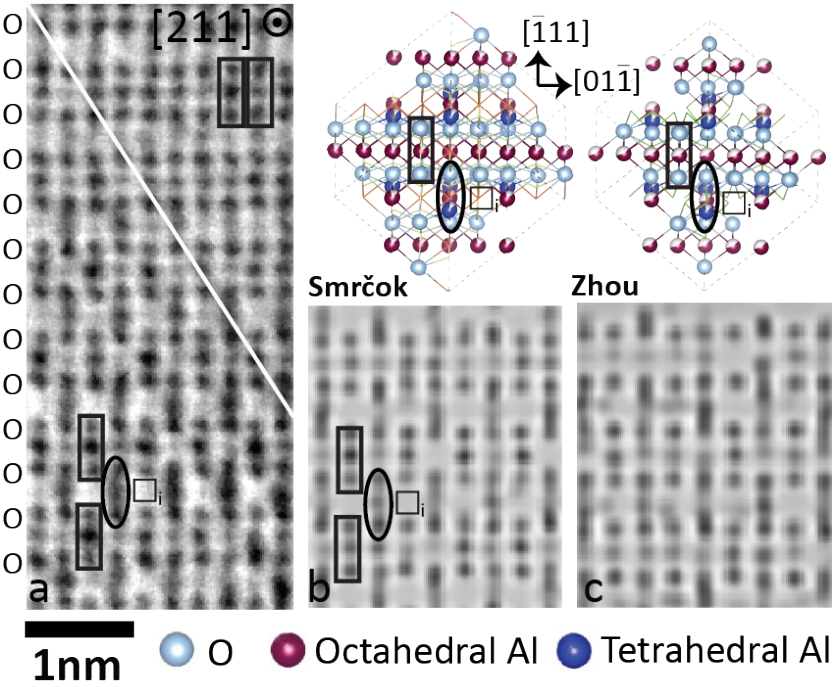

Figure 5 *(a) Detail from Figure 4(b) highlighting apparent ɣ-alumina variants. The white line indicates the approximate boundary between the variants. Column (b) shows the Smrčok unit cell and ABF image simulation and column (c) shows the same for the Zhou model. (a-c) are viewed on [211] zone axis and are to the same scale. Groups of O-Al_o-O columns are marked with boxes , O-Al_{mix}-O groups with ovals, and interstitial sites with low occupancy Al with $\square_i$ in the models and simulations, aiding in the*

interpretation of the experimental structure. The {111} layers identified as part of the O-sub-lattice are labelled at the left with Os.

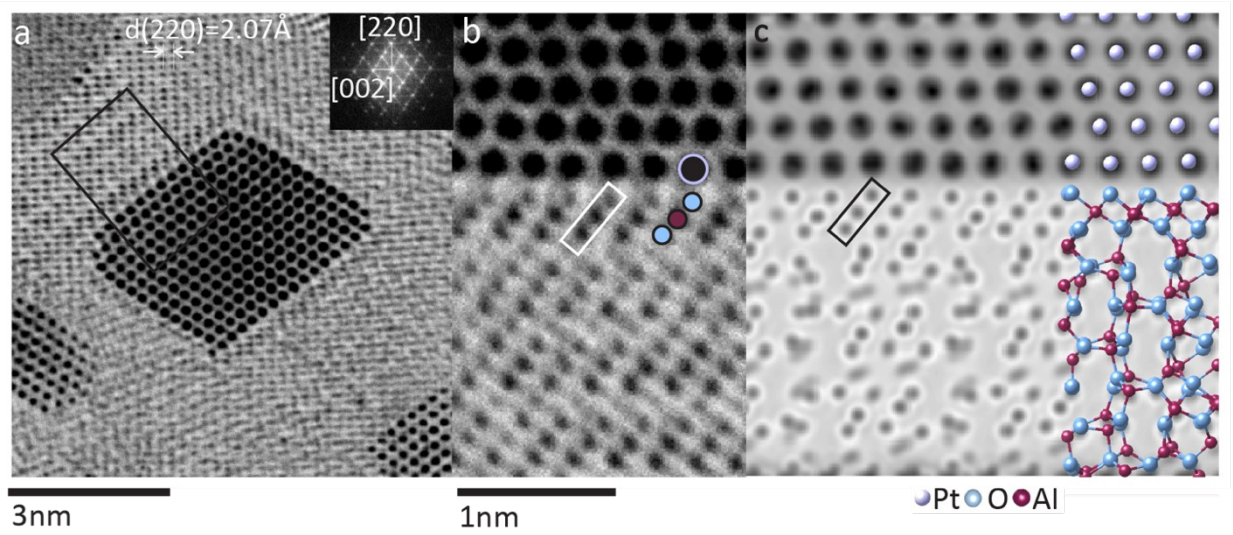

Figure *6* *(a) Drift-corrected ABF STEM image of a Pt NP in ɣ-alumina imaged along the $[110]_{Pt}$ zone-axis (STEM probe step size: 0.0083 nm). The Pt NP is bound by (111)Pt/ɣ-alumina interfaces. The boxed region in (a) is enlarged in (b). (c) Simulated ABF STEM images of the Oware Sarfo O-terminated interface with the model overlaid on the right. There is an excellent match between the experimental images and the simulated images of the O-terminated model interface up to the first three atomic layers of alumina (O-Al_o-O).*

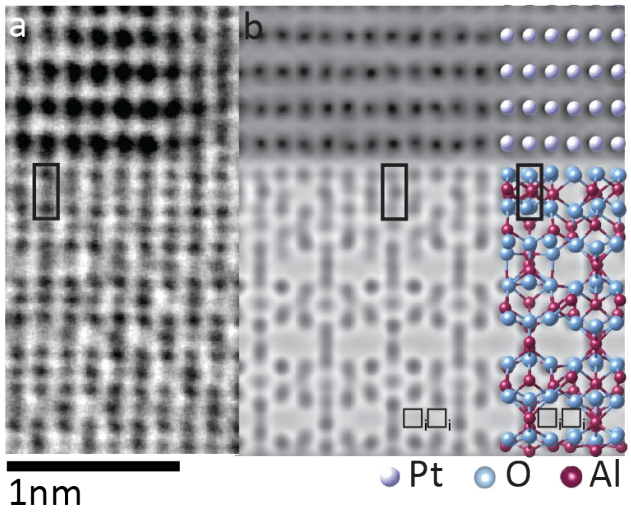

Figure 7 *(a) Detail of ABF image boxed region in Figure 4(b) viewed on a $[211]_{Pt}$ zone-axis. (b) Simulated STEM ABF image the Oware Sarfo O-terminated interface with the model overlaid on the right at the same scale as (a). Groups of O-Al_o-O columns are marked with black rectangles and adjacent columns of completely unoccupied interstitial sites are marked in the model and simulation with $□_i□_i$.*

Table 2 *Pt and γ-Al_2O_3 lattice parameters*

	Lattice parameter (nm)
Pt (this work)	0.416 ± 0.001
Bulk Pt [51]	0.3912
γ-alumina (this work)	0.822 ± 0.016
Smrčok γ-alumina	0.79382(1)
Zhou γ-alumina	0.7911(2)

Table 3 *Pt-O distances measured at the interfaces of the Oware Sarfo models and in atomic resolution STEM images*

Interface	**Pt-O plane-to-plane distance (nm)**
O-terminated model	0.196
Al_1-terminated model	0.239
Al_2-terminated model	0.327
experiment	0.205 ± 0.020

References

1 C.R. Henry, Surface studies of supported model catalysts, Surface Science Reports 31(7-8) (1998) 231-325.
2 P. Raybaud, C. Chizallet, C. Mager-Maury, M. Digne, H. Toulhoat, P. Sautet, From γ-alumina to supported platinum nanoclusters in reforming conditions: 10 years of DFT modeling and beyond, Journal of Catalysis 308 (2013) 328-340.
3 V.P. Pakharukova, I.Y. Pakharukov, V.I. Bukhtiyarov, V.N. Parmon, Alumina-supported platinum catalysts: Local atomic structure and catalytic activity for complete methane oxidation, Applied Catalysis A: General 486 (2014) 12-18.
4 L. He, Y.L. Fan, L.G. Luo, J. Bellettre, J. Yue, Preparation of Pt/γ-Al_2O_3 catalyst coating in microreactors for catalytic methane combustion, Chemical Engineering Journal 380 (2020) 18.
5 S. Mostafa, F. Behafarid, J.R. Croy, L.K. Ono, L. Li, J.C. Yang, A.I. Frenkel, B. Roldan Cuenya, Shape-dependent catalytic properties of Pt nanoparticles, Journal of the American Chemical Society 132(44) (2010) 15714-15719.
6 M. Arenz, K.J.J. Mayrhofer, V. Stamenkovic, B.B. Blizanac, T. Tomoyuki, P.N. Ross, N.M. Markovic, The Effect of the Particle Size on the Kinetics of CO Electrooxidation on High Surface Area Pt Catalysts, Journal of the American Chemical Society 127(18) (2005) 6819-6829.
7 J.H. Kwak, J. Hu, D. Mei, C.-W. Yi, D.H. Kim, C.H.F. Peden, L.F. Allard, J. Szanyi, Coordinatively unsaturated Al_3^+ centers as binding sites for active catalyst phases of platinum on γ-Al_2O_3, Science 325(5948) (2009) 1670-1673.
8 W.G. Rothschild, H.C. Yao, H.K. Plummer, Surface interaction in the Pt/γ-Al_2O_3 system 5. Effects of atmosphere and fractal topology on the sintering of Pt, Langmuir 2(5) (1986) 588-593.
9 S.M. Augustine, W.M.H. Sachtler, Variation of catalytic activity over PtRe/γ-Al_2O_3, J. Phys. Chem. 91(23) (1987) 5953-5956.
10 A. Dandapat, D. Jana, G. De, Synthesis of Thick Mesoporous γ-Alumina Films, Loading of Pt Nanoparticles, and Use of the Composite Film as a Reusable Catalyst, ACS Applied Materials & Interfaces 1(4) (2009) 833-840.
11 C. Mager-Maury, C. Chizallet, P. Sautet, P. Raybaud, Platinum Nanoclusters Stabilized on γ-Alumina by Chlorine Used As a Capping Surface Ligand: A Density Functional Theory Study, ACS Catalysis 2(7) (2012) 1346-1357.
12 M.W. Small, S.I. Sanchez, L.D. Menard, J.H. Kang, A.I. Frenkel, R.G. Nuzzo, The atomic structural dynamics of γ-Al_2O_3 supported Ir-Pt nanocluster catalysts prepared from a bimetallic molecular precursor: a study using aberration-corrected electron microscopy and X-ray absorption spectroscopy, Journal of the American Chemical Society 133(10) (2011) 3582-3591.
13 L. Kovarik, A. Genc, C.M. Wang, A.N. Qiu, C.H.F. Peden, J. Szanyi, J.H. Kwak, Tomography and High-Resolution Electron Microscopy Study of Surfaces and Porosity in a Plate-like γ-Al_2O_3, Journal of Physical Chemistry C 117(1) (2013) 179-186.
14 Z. Zhang, L. Li, J.C. Yang, Adhesion of Pt Nanoparticles Supported on γ-Al_2O_3 Single Crystal, Journal of Physical Chemistry C 117(41) (2013) 21407-21412.
15 H.O. Ayoola, C.S. Bonifacio, Q. Zhu, C.H. Li, S.D. House, J.J. Kas, J. Jinschek, J.J. Rehr, W.A. Saidi, J.C. Yang, Probing the Local Bonding at the Pt/γ-Al_2O_3 Interface, Journal of Physical Chemistry C 124(18) (2020) 9876-9885.
16 H.O. Ayoola, C.H. Li, S.D. House, C.S. Bonifacio, K. Kisslinger, J. Jinschek, W.A. Saidi, J.C. Yang, Origin and suppression of beam damage-induced oxygen-K edge artifact from γ-Al_2O_3 using cryo-EELS, Ultramicroscopy 219 (2020) 113127.

17 E.J.W. Verwey, The structure of the electrolytical oxide layer on aluminium, Zeitschrift für Kristallographie - Crystalline Materials 91(3/4) (1935) 317-320.
18 S.J. Wilson, Dehydration of boehmite, γ-AlOOH, to γ-Al_2O_3, Journal of Solid State Chemistry 30(2) (1979) 247-255.
19 R.S. Zhou, R.L. Snyder, Structures and transformation mechanisms of the eta, γ, and θ transitions aluminas, Acta Crystallographica Section B-Structural Science 47 (1991) 617-630.
20 X. Krokidis, P. Raybaud, A.E. Gobichon, B. Rebours, P. Euzen, H. Toulhoat, Theoretical study of the dehydration process of boehmite to γ-alumina, Journal of Physical Chemistry B 105(22) (2001) 5121-5130.
21 M. Digne, P. Sautet, P. Raybaud, P. Euzen, H. Toulhoat, Hydroxyl groups on γ-alumina surfaces: A DFT study, Journal of Catalysis 211(1) (2002) 1-5.
22 G. Gutierrez, A. Taga, B. Johansson, Theoretical structure determination of γ-Al_2O_3, Phys. Rev. B 65(1) (2001) 012101.
23 G. Paglia, C.E. Buckley, A.L. Rohl, B.A. Hunter, R.D. Hart, J.V. Hanna, L.T. Byrne, Tetragonal structure model for boehmite-derived γ-alumina, Phys. Rev. B 68(14) (2003) 144110.
24 M. Digne, P. Sautet, P. Raybaud, P. Euzen, H. Toulhoat, Use of DFT to achieve a rational understanding of acid-basic properties of γ-alumina surfaces, Journal of Catalysis 226(1) (2004) 54-68.
25 H.P. Pinto, R.M. Nieminen, S.D. Elliott, Ab initio study of γ-Al_2O_3 surfaces, Phys. Rev. B 70(12) (2004) 125402.
26 L. Smrcok, V. Langer, J. Krestan, Gamma-alumina: a single-crystal x-ray diffraction study, Acta Crystallographica Section C-Structural Chemistry 62 (2006) I83-I84.
27 K. Wefers, C. Misra, Oxides and Hydroxides of Aluminum: Alcoa Technical Paper No. 19, Revised Alcoa Laboratories, 1987.
28 H.S. Potdar, K.-W. Jun, J.W. Bae, S.-M. Kim, Y.-J. Lee, Synthesis of nano-sized porous gamma-alumina powder via a precipitation/digestion route, Appl. Catal. A-Gen. 321(2) (2007) 109-116.
29 Y. Liu, D. Ma, X.W. Han, X.H. Bao, W. Frandsen, D. Wang, D.S. Su, Hydrothermal synthesis of microscale boehmite and γ nanoleaves alumina, Materials Letters 62(8-9) (2008) 1297-1301.
30 S. Lan, N. Guo, L. Liu, X.M. Wu, L.L. Li, S.C. Gan, Facile preparation of hierarchical hollow structure gamma alumina and a study of its adsorption capacity, Appl. Surf. Sci. 283 (2013) 1032-1040.
31 I. Levin, T. Gemming, D.G. Brandon, Some metastable polymorphs and transient stages of transformation in alumina, Phys. Status Solidi A-Appl. Res. 166(1) (1998) 197-218.
32 C.W. White, C.J. McHargue, P.S. Sklad, L.A. Boatner, G.C. Farlow, Ion implantation and annealing of crystalline oxides, Material Science Reports 4(2-3) (1989) 41-146.
33 A.L. Clauser, R. Giulian, Z.D. McClure, K. Oware Sarfo, C. Ophus, J. Ciston, L. Arnadottir, M.K. Santala, Orientation and morphology of Pt nanoparticles in γ-alumina processed via ion implantation and thermal annealing, Scr. Mater. 188 (2020) 44-49.
34 J.C. Yang, E. Schumann, I. Levin, M. Ruhle, Transient oxidation of NiAl, Acta Materialia 46(6) (1998) 2195-2201.
35 H.O. Ayoola, S.D. House, C.S. Bonifacio, K. Kisslinger, W.A. Saidi, J.C. Yang, Evaluating the accuracy of common γ-Al_2O_3 structure models by selected area electron diffraction from high-quality crystalline γ-Al_2O_3, Acta Materialia 182 (2020) 257-266.
36 J. Krest'an, O. Pritula, L. Smrcok, P. Sajgalik, Z. Lences, A. Wannberg, F. Monteverde, Corrosion of beta-sialon-based ceramics by molten steel, Journal of the European Ceramic Society 27(5) (2007) 2137-2143.
37 L. Kovarik, M. Bowden, A. Genc, J. Szanyi, C.H.F. Peden, J.H. Kwak, Structure of δ-Alumina: Toward the Atomic Level Understanding of Transition Alumina Phases, The Journal of Physical Chemistry C 118(31) (2014) 18051-18058.
38 M. Ahmadi, F. Behafarid, B. Roldan Cuenya, Size-dependent adhesion energy of shape-selected Pd and Pt nanoparticles, Nanoscale 8(22) (2016) 11635-11641.

39 C.W. White, L.A. Boatner, P.S. Sklad, C.J. McHargue, J. Rankin, G.C. Farlow, M.J. Aziz, Ion-Implantation and Annealing of Crystalline Oxides and Ceramic Materials, Nuclear Instruments & Methods in Physics Research Section B-Beam Interactions with Materials and Atoms 32(1-4) (1988) 11-22.
40 J.D. Budai, C.W. White, S.P. Withrow, M.F. Chisholm, J. Zhu, R.A. Zuhr, Controlling the size, structure and orientation of semiconductor nanocrystals using metastable phase recrystallization, Nature 390(6658) (1997) 384-386.
41 M. Gandman, M. Ridgway, R. Gronsky, A.M. Glaeser, Microstructural evolution in Pt-implanted polycrystalline Al_2O_3, Acta Materialia 83 (2015) 169-179.
42 P. Eklund, M. Sridharan, G. Singh, J. Bottiger, Thermal Stability and Phase Transformations of γ-/Amorphous-Al_2O_3 Thin Films, Plasma Processes and Polymers 6 (2009) S907-S911.
43 S. Lamouri, M. Hamidouche, N. Bouaouadja, H. Belhouchet, V. Garnier, G. Fantozzi, J.F. Trelkat, Control of the γ-alumina to α-alumina phase transformation for an optimized alumina densification, Boletín de la Sociedad Española de Cerámica y Vidrio 56(2) (2017) 47-54.
44 I. Levin, D. Brandon, Metastable alumina polymorphs: Crystal structures and transition sequences, Journal of the American Ceramic Society 81(8) (1998) 1995-2012.
45 K. Oware Sarfo, A.L. Clauser, M.K. Santala, L. Árnadóttir, On the atomic structure of Pt(111)/γ-Al_2O_3(111) interfaces and the changes in their interfacial energy with temperature and oxygen pressure, Appl. Surf. Sci. 542 (2021) 148594.
46 N.A. Deskins, D.H. Mei, M. Dupuis, Adsorption and diffusion of a single Pt atom on γ-Al_2O_3 surfaces, Surface Science 603(17) (2009) 2793-2807.
47 C. Mager-Maury, G. Bonnard, C. Chizallet, P. Sautet, P. Raybaud, H-2-Induced Reconstruction of Supported Pt Clusters: Metal-Support Interaction versus Surface Hydride, ChemCatChem 3(1) (2011) 200-207.
48 C. Ophus, J. Ciston, C.T. Nelson, Correcting nonlinear drift distortion of scanning probe and scanning transmission electron microscopies from image pairs with orthogonal scan directions, Ultramicroscopy 162 (2016) 1-9.
49 L.R. DaCosta, G.H. Brown, M.P. Pelz, A. Rakowski, N. Barber, P. O'Donovan, P. McBean, L. Jones, J. Ciston, M.C. Scott, C. Ophus, Prismatic 2.0-Simulation software for scanning and high resolution transmission electron microscopy (STEM and HRTEM), Micron 151 (2021) 103141.
50 M. Nord, P.E. Vullum, I. MacLaren, T. Tybell, R. Holmestad, Atomap: a new software tool for the automated analysis of atomic resolution images using two-dimensional Gaussian fitting, Adv Struct Chem Imaging 3(1) (2017) 9.
51 W.P. Davey, Precision Measurements of the Lattice Constants of Twelve Common Metals, Physical Review 25(6) (1925) 753-761.
52 R. Giulian, P. Kluth, L.L. Araujo, D.J. Llewellyn, M.C. Ridgway, Pt nanocrystals formed by ion implantation: A defect-mediated nucleation process, Appl. Phys. Lett. 91(9) (2007).
53 R. Giulian, L.L. Araujo, P. Kluth, D.J. Sprouster, C.S. Schnohr, B. Johannessen, G.J. Foran, M.C. Ridgway, The influence of annealing conditions on the growth and structure of embedded Pt nanocrystals, J. Appl. Phys. 105(4) (2009).
54 C.W. White, S.P. Withrow, J.D. Budai, D.K. Thomas, J.M. Williams, A. Meldrum, K.D. Sorge, J.R. Thompson, G.W. Ownby, J.F. Wendelken, L.A. Boatner, Annealing-environment effects on the properties of CoPt nanoparticles formed in single-crystal Al_2O_3 by ion implantation, J. Appl. Phys. 98(11) (2005) 114311
55 H.J. Wasserman, J.S. Vermaak, Determination of surface stress of copper and platinum, Surface Science 32(1) (1972) 168-174.
56 C. Solliard, M. Flueli, Surface stress and size effect on the lattice-parameter in small particles of gold and platinum, Surface Science 156(Jun) (1985) 487-494.

57 M. Klimenkov, S. Nepijko, H. Kuhlenbeck, M. Baumer, R. Schlogl, H.J. Freund, The structure of Pt-aggregates on a supported thin aluminum oxide film in comparison with unsupported alumina: a transmission electron microscopy study, Surface Science 391(1-3) (1997) 27-36.
58 K. Du, F. Emst, M.C. Pelsozy, J. Barthel, K. Tillmann, Expansion of interatomic distances in platinum catalyst nanoparticles, Acta Materialia 58(3) (2010) 836-845.
59 J.R. Gallagher, T. Li, H.Y. Zhao, J.J. Liu, Y. Lei, X.Y. Zhang, Y. Ren, J.W. Elam, R.J. Meyer, R.E. Winans, J.T. Miller, In situ diffraction of highly dispersed supported platinum nanoparticles, Catalysis Science & Technology 4(9) (2014) 3053-3063.
60 I.N. Leontyev, A.B. Kuriganova, N.G. Leontyev, L. Hennet, A. Rakhmatullin, N.V. Smirnova, V. Dmitriev, Size dependence of the lattice parameters of carbon supported platinum nanoparticles: X-ray diffraction analysis and theoretical considerations, Rsc Advances 4(68) (2014) 35959-35965.
61 C. Liu, G. Li, D.R. Kauffman, G.S. Pang, R.C. Jin, Synthesis of ultrasmall platinum nanoparticles and structural relaxation, J. Colloid Interface Sci. 423 (2014) 123-128.
62 S.N. Khanna, J.P. Bucher, J. Buttet, F. Cyrotlackmann, Stability and lattice contraction of small platinum particles, Surface Science 127(1) (1983) 165-174.
63 W.H. Qi, B.Y. Huang, M.P. Wang, Z.M. Yin, J. Li, Molecular dynamic simulation of the size- and shape-dependent lattice parameter of small Platinum nanoparticles, Journal of Nanoparticle Research 11(3) (2009) 575-580.
64 R.V. Chepulskii, S. Curtarolo, Ab Initio Insights on the Shapes of Platinum Nanocatalysts, Acs Nano 5(1) (2011) 247-254.
65 C. Ophus, M.K. Santala, M. Asta, V. Radmilovic, Structure and phase transitions at the interface between α-Al_2O_3 and Pt, Journal of Physics: Condensed Matter 25 (2013) 232202.